Anal Bioanal Chem (2014) 406:6993–7002
DOI 10.1007/s00216-014-7998-y

RESEARCH PAPER

Label-free in vitro visualization and characterization of caveolar bulbs during stimulated re-epithelialization

Melissa Watkins-Mariani · Tanja Deckert-Gaudig · Volker Deckert

Received: 7 April 2014 / Revised: 19 June 2014 / Accepted: 24 June 2014 / Published online: 11 July 2014

Abstract Tip-enhanced Raman scattering (TERS) was paired with real-time reverse transcription quantitative polymerase chain reaction (RT-qPCR) to characterize lipid aggregates during stimulated re-epithelialization using an in vitro wound healing model. In this study, lipid fluctuations in the plasma membrane of epidermal keratinocytes were studied at multiple time points post-wounding. TERS measurements for the first time were also combined with sample analysis after initial wounding and 24 h of wound healing. This enabled simultaneous visualization and characterization of caveolar bulb distribution during wound healing stages, providing noninvasive insight into their associated lipid structure and coating protein, caveolin, in the nanometer range. The combination of Raman spectroscopy and scanning probe microscopy in TERS gives access to topographic and chemical structure information in a single experiment. It is the intrinsic specificity and sensitivity of TERS that enable this discrete detection of cell surface components on the nanometer scale. In contrast with competing biochemical methods, the applied technique does not interfere with the cellular composition, enabling lipid structure analysis without digestion or detergents, and displayed great potential for future biological in vivo studies.

Keywords TERS · Caveolae · Caveolin · Wound healing · Sphingolipid

Introduction

Cell polarization is a vital developmental process, taking place during developmental stages, multicellular tissue formation, and wound healing. Epithelia are the archetypal model of polarized tissue, with over 60 % of mammalian cell types stemming from epithelial or epithelial-derived origin. Not only is the process of cell polarization vital to organism development, deviations in proper polarization have also been linked to cancer manifestations, along with other diseases [1]. Polarization can occur in the apical/basal and proximal/distal axes, with many cellular components responding in association to these cues [2]. As the precise mechanisms that direct cell polarization remain poorly understood [3], better elucidation of structural cell responses to polarization cues and their chemical compositions can provide insight into downstream mechanistic occurrences.

The plasma membrane is the barrier between cytoplasmic components and the surrounding environment. This fluid bilayer is fabricated predominately of lipids, enabling the structure to rearrange in response to environmental cues. Plasma membrane lipid dynamics and their importance in mediating cell functions, like signal transduction pathways [4, 5] and vesicular transport [6], have become of increasing interest. Lipid aggregates have received the most attention from their influence on regulating cell membrane functions, disease pathogenesis, and general organism physiology, particularly through the formation of subcompartments. These inclusions, like caveolar bulbs, are understood to dynamically

---

Published in the topical collection *Single Cell Analysis* with guest editors Petra Dittrich and Norbert Jakubowski.

Electronic supplementary material The online version of this article (doi:10.1007/s00216-014-7998-y) contains supplementary material, which is available to authorized users.

M. Watkins-Mariani
East 42nd Street, New York, NY 10017, USA

T. Deckert-Gaudig · V. Deckert (✉)
IPHT–Leibniz Institute for Photonic Technology,
Albert-Einstein-Str. 9, 07743 Jena, Germany
e-mail: volker.deckert@uni-jena.de

V. Deckert
IPC–Friedrich-Schiller-University of Jena and Abbe Center of
Photonics, Helmholtzstr. 4, 07743 Jena, Germany

regulate migratory activity [4] and recruit signaling molecules into lipid microdomains during wound healing stages [5, 6]. From their widespread involvement in polarization and subsequent migratory activity, such inclusions specifically have become of great interest but remain poorly characterized [6–8]. In particular, caveolar bulbs are an intriguing model to examine membrane protein interactions with lipids for their influence on membrane morphogenesis and generation of lipid microdomains [7, 9].

Caveolar bulbs possess a diameter spanning 50–100 nm [10, 11], although they can be larger (up to 1 μm) when multiple bulbs combine to form so-called caveosomes and become widespread on cell membranes in subsequent stages after initial wound healing [10, 12, 13]. Several methods have been explored to visualize their structure, including transmission and scanning electron microscopy, scanning force microscopy, and immunofluorescence, to better understand their involvement in wound healing [7, 9, 11, 13]. Examples include techniques like detergent-resistant membrane fraction analysis [14], labeling through the use of fluorescent probes [10, 15], or spectroscopic investigations using FT-IR which have all been attempted. Combined, these techniques successfully analyze lipid content but possess similar setbacks based on their applied resolution and ability to maintain native analyte structures, rendering spatiotemporal insight paired with biochemical information of great difficulty to obtain [16].

Considering traditional lipid analysis methodology and limitations, tip-enhanced Raman scattering (TERS) was applied. This technique was selected for its provision of ultrasensitive structural characterization and nanometer-level resolution. TERS spectroscopy is an emergent spectroscopic technique, integrating the recognized methodology of surface-enhanced Raman scattering (SERS) and scanning probe technologies. In SERS, the low sensitivity of Raman spectroscopy is overcome by adsorption of the sample on rough metal surfaces like silver or gold (see ref. [17, 18]). Drawbacks of SERS include a lack in spatial resolution, which is easily overcome with TERS through reducing the enhancing unit to a single nanoparticle. TERS also applies the near-field enhancements characteristic of SERS through the illumination of single silver or gold particles attached to the tip of an atomic force microscope (AFM) or scanning tunneling microscope (STM). For detailed examples, the reader is referred to the following reviews [19–21] and literature cited therein. Depending on the particle shape and size, enhancement factors of the Raman scattering can reach several orders of magnitude, resulting in a highly resolved structural analysis. Recent studies have applied TERS to the surface of cells, bacteria, and viruses, reinforcing the capability of TERS for cell membrane studies [22–24].

Here, the involvement of lipids in keratinocyte re-epithelialization was explored using TERS and was further verified with "gold standard" techniques like immunohistochemistry and real-time reverse transcription quantitative polymerase chain reaction (RT-qPCR) for the transcriptome. For the first time, caveolar bulb distribution was imaged with TERS and their chemical structure was analyzed. Moreover, this label-free, molecule-sensitive technique exhibited its improved sensitivity and unprecedented resolution, outperforming the routine biological counterparts.

Materials and methods

Cell culture The established human-derived epidermal keratinocyte cell line (HaCaT cells) was cultured in Dulbecco's minimal Eagle's medium (DMEM) (PAA, Germany), supplemented with 1 % GlutaMax (Invitrogen) and 10 % fetal bovine serum (Invitrogen) and in the presence of 1,000 units/mL penicillin and 1,000 units/mL streptomycin (Invitrogen) at 37 °C with 5 % CO_2 in air. Upon confluency, HaCaT cells were trypsinized with 0.25 % Trypsin+ETDA (Invitrogen). Trypsin was inactivated with a 1:4 dilution of media, and cells were pelleted for use by centrifugation at 400*g* for 5 min.

Simulated wounding sample preparation Samples were prepared as described above. Following swift insert removal, wounded samples were cultured in DMEM until each predetermined time point (0, 24, and 36 h). Time 0 reflects sample fixation immediately following insert removal. At each time point, samples were washed with sterile phosphate-buffered saline (PBS) and fixed with 2 % formaldehyde in PBS for 1 h. Samples were then wrapped in foil and stored at −80 °C until used.

TERS Detailed TERS instrumentation has been previously described [23]. Briefly, 20 nm of silver (99.99 % pure, Balzers Materials, Liechtenstein) coated a noncontact-mode silicon cantilever AFM tip (NSG10, NT-MDT, Russia) by thermal evaporation (BAL-TEC MDS 020 BAL-TEC GmbH, Liechtenstein) using an evaporation rate of 0.06 nm s^{-1}. Tips were stored under argon until used within 2 days. For the measurements, a back reflection setup based on an inverted Raman microscope (LabRAM HR, Horiba, France) and an AFM mounted on top of the light path (NanoWizard I, JPK, Germany) was employed. A 568 nm laser light (laser power after last lens: 0 h sample, $P=750$ μW; 24 h sample, $P=1.1$ mW) was focused through a 60× oil immersion objective (N.A.=1.45) and the sample on the tip. The acquisition times were set as follows: 0 h sample, $t_{acq}=10$ s, and 24 h sample, $t_{acq}=15$ s. All shown spectra are raw spectra.

RNA extraction RNA was extracted at all time points from the entire sample following the manufacturer's protocol supplied in the RNA Mini Kit (Qiagen). Briefly, cells were lysed in lysis buffer and vortexed for sample homogenization. Samples were centrifuged at 8,000*g* for 30 s to remove gDNA, and the flow-through was mixed with 70 % ethanol. The samples were transferred to spin columns that bind total RNA during centrifugation at 8,000*g* for 15 s. All total RNA bound to the spin-filter was cleaned of residual ethanol by additional centrifugation at 8,000*g* for 15 s. Samples were then washed with 80 % ethanol, centrifuged at 8,000*g* for 2 min, and dried by centrifugation at 25,000*g* for 5 min. Total RNA was then eluted from the spin column into RNase-free water by centrifugation at 25,000*g* for 1 min. RNA quality was assessed by automated gel electrophoresis (Bio-Rad, Germany) with RNA StdSens chips, and the concentration was confirmed using a NanoDrop® ND-1000 UV/visible spectrophotometer (NanoDrop Technologies Ltd, USA).

cDNA synthesis Reverse transcription was performed using SuperScript III reverse transcriptase (Invitrogen, Dorset, UK) as specified by the manufacturer. To begin with, 200 ng of total RNA was combined with 0.5 µg oligo-dT$_{12–18}$ (Invitrogen) and 10 mM dNTP mix (Invitrogen), incubated for 5 min at 65 °C, and then chilled on ice. Samples were then combined with 4 µL 5× first strand buffer (containing 250 mM Tris–HCI (pH 8.3), 375 mM KC1, 15 mM MgCl$_2$), 1 µL of 0.1 M DTT, 40 units of RNAse (Promega), and 200 units of SuperScript II reverse transcriptase (Invitrogen). Once combined, samples were incubated for 60 min at 50 °C. The enzymatic activity of reverse transcriptase was ceased by sample incubation at 70 °C for 15 min. Samples were stored at −80 °C until subsequent use.

RT-qPCR Candidate genes were selected from a previous microarray screening and from relevant literature. Reference genes specific to the cell line were previously determined by identifying the two most stable genes from the 12 most stable suggested by Vandesompele et al. [25].

All RNA transcript sequences were acquired online from the National Centre for Biotechnology Information. Transcripts were cross-referenced with corresponding Ensembl Human Genome Database sequences. Homologous regions were then used for primer and probe assay design using the Universal ProbeLibrary Assay Design Centre (Roche Diagnostics Ltd). Subsequent BLAST searches were performed for all sequences to confirm primer-gene specificity. Primers were then synthesized by Metabion (Germany) and probes were synthesized by Roche Diagnostics (UK), implementing the locked nucleic acid technology, and

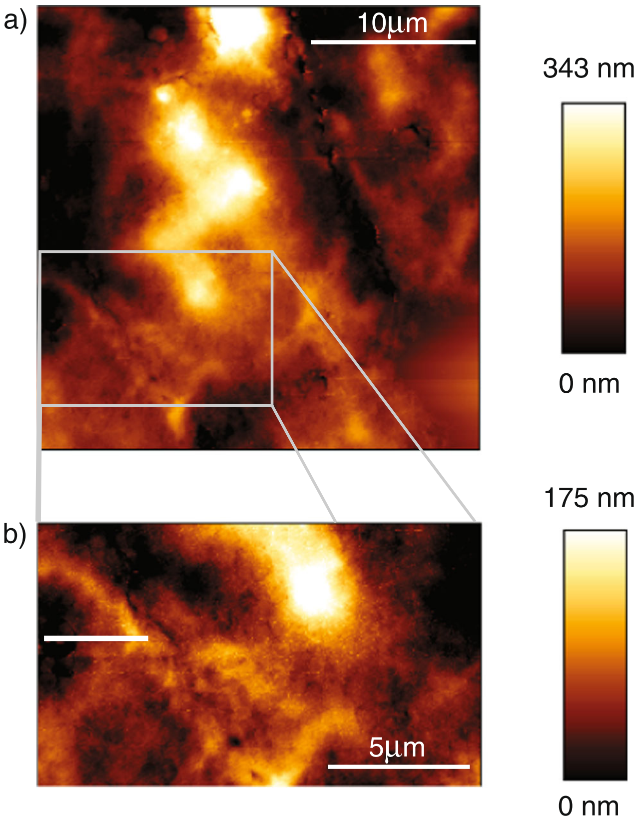

Fig. 1 **a** AFM topography of a HaCaT cell immediately after wounding (0 h); **b** enlarged image with the *white line* indicating the region of TERS measurement

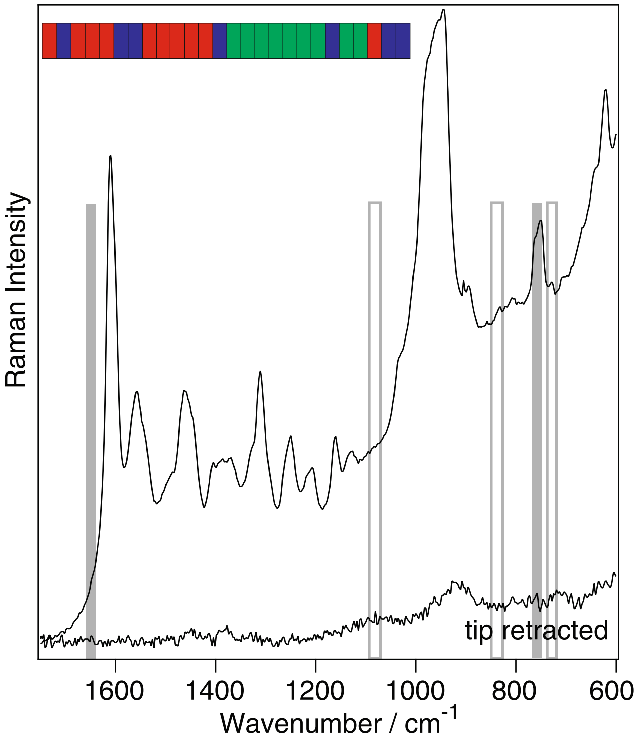

Fig. 2 Average TERS spectrum of 26 raw spectra on a HaCaT cell initially after wounding (0 h); distance of measured points, 150 nm, t_{acq}=10 s. Marker bands are highlighted; *grey line* protein, *rectangle* lipid. A reference spectrum of the cell was acquired (10 s) with 500 µm retracted tip; the *colored map* shows the detection of proteins (*red*), lipids (*green*), and mixtures of both (*blue*) along the measured line

incorporated the reporter dye fluorescein (FAM (6-carboxy fluorescene)) at the 5′-end and the dark quencher dye at the 3′-end.

Every RT-qPCR assay was performed in triplicate using the 384-well configuration and an ABI® 7900 (Applied Biosciences, Germany). Each assay included three no-template controls. The reaction volume for each well was 10 μL and contained 5 μL 2× Precision Master Mix (Primer Design, UK). Additionally, 0.7 μL of RNase-free H_2O (Ambion, Inc.), 0.1 μL of 20 μM forward primer, 0.1 μL of 20 μM reverse primer, 0.1 μL of 10 μM Roche fluorescently labeled probe, and 4 μL of sample complementary DNA (cDNA) at 2.5 ng/μL were added to each well. All no-template control wells supplemented cDNA volume with 4 μL of RNase-free H_2O. The amplification conditions for all assays included 1 cycle at 65 °C for 5 min and 40 cycles at 95 °C for 2 min, 95 °C for 15 s, and 60 °C for 1 min. RT-qPCR data were analyzed by using ABI® 7900 standard software to determine cycle threshold values (Ct) and relatively quantified to the time 0 gene expression profiles to determine changes during re-epithelialization.

Statistical analysis RT-qPCR data were assessed for statistical significance using the $2^{\Delta\Delta Ct}$ values following relative quantification for each candidate gene. These transformed values for each gene were then imported into GraphPad Prism software (version 3.0) and assessed for significance using the Mann-Whitney *U* nonparametric test, with a 90 % confidence interval, to assess whether the genetic distributions of the two time points were statistically significant ($N=3$ for each time point, $N=3$ for each RT-qPCR gene replicate).

Immunofluorescence After fixation and spectroscopic analysis, cell samples were labeled with FITC (fluorescein isothiocyanate) for caveolin-1. To accomplish this, samples were rehydrated in PBS for 5 min and then blocked for 30 min with 1 % bovine serum albumin (BSA) in PBS+Tween (PBST) to prohibit nonspecific antibody binding. For visualization of caveolin lipid invaginations and the plasma membrane, cells were labeled with rabbit polyclonal caveolin-1 (abcam, UK) at a concentration of 5 μg/mL for 1 h at room temperature. Samples were washed three times for 5 min each and stained with the corresponding secondary antibodies. Goat anti-rabbit IgG FITC conjugate (abcam, UK) was used at a concentration of 40 μg/mL and incubated for 1 h at room temperature. Samples were then washed three times for 5 min each

Table 1 Band assignment for TERS spectra on a HaCaT cell just after wounding (0 h)

Wavenumber/cm^{-1}	Assignment	Reference
1,647, 1,636	Amide I (prot), C=C str. (lipid)	[22, 28]
1,614, 1,589	C=C stretch (prot), C=C str. (lipid)	[22, 23]
1,573–1,558, 1,529, 1,513	Amide II, C=C str. (prot)	[22, 23, 28]
1,494, 1,487, 1,468	CH_2, CH_3 def. (lipid, prot)	[22]
1,451, 1,441	CH_2 str. (lipid, prot)	[22]
1,414, 1,407, 1,390, 1,377, 1,353, 1,342, 1,329	CH_2, CH_3 bend (lipid, prot)	[22, 23]
1,312	CH_2 twist (lipid)	[22, 23, 29]
1,295, 1,270	Amide III (prot), =CH bend (lipid)	[22]
1,250, 1,224	Amide III (prot), PO_2 asym. str. (lipid)	[22, 23, 29]
1,218, 1,207	CH str. (prot)	[22]
1,163	C–O str., C–OH, bend, CH bend, CCN (prot)	[22, 23]
1,135, 1,119	C–C str. (lipid, prot), C–N str. (prot)	[22, 23]
1,092, 1,085	C–C str., C–O str., PO_2 sym. str. (lipid)	[22, 23]
1,038	C–OH str. (lipid)	[22, 23]
1,009	Ring breath (phe, prot)	[22, 23]
990–920	Si overtone of tip	
896, 888	C–C str. residue, CH bend (prot)	[22, 23]
852	Ring breath (tyr, prot)	[22, 23]
834	PO_2 asym str., CH (lipid)	[22, 23]
804, 774, 750	C–S str. (prot.)	[22, 23]
728	Me_3N^+ sym str. (sphingolipid)	[30, 31]
706	Ring breath (cholesterol)	[29, 32]
648	?	
620	Ring def. (phe, prot), amide IV	[22, 23]

with PBS, and the nuclei were counterstained with 14′,6-diamidino-2-phenylindole (DAPI) (Sigma-Aldrich, Germany) at 1:1,000 dilution for 2 min. Samples were again washed three times for 5 min each and mounted (Sigma-Aldrich, Germany).

An Olympus IX70 wide-field fluorescence microscope (Olympus, Japan) was used with appropriate bandpass filters for 350–460 nm (DAPI) and 510–540 nm (FITC). Images were captured using Cell^A software (Olympus, Japan) and a Canon 35-mm CCD system.

Results and discussion

Histological staining

Previous studies have mentioned the importance of lipids during cell polarization, particularly during cell migration [26, 27], but none have been capable of breaking down the composition and rearrangements of these components during the polarization of intact cells. For comparison with commonplace histological methods, samples were dual-labeled for lipid content using the histological stain Oil Red O and for the nucleus using DAPI. The result of this traditional staining was unable to clearly identify regions of lipid content amongst keratinocyte monolayers from their lack of red-stained lipid-specific regions (see Electronic Supplementary Material (ESM) Fig. S1). Traditional histological staining was also not able to provide a spatial resolution high enough to differentiate between fatty acid types. In turn, spectroscopy was applied to further differentiate plasma membrane lipid fluctuations during polarization, while providing an increased spatial resolution and sensitivity.

TERS studies

To obtain topographical insight into the lipid organization of the plasma membrane, TERS was applied to keratinocytes initially following stimulated wounding (0 h) and during migratory activity, where cells are distinctly polarized (24 h). Figure 1a displays the topography of an individual cell from the edge of the induced wound obtained at 0 h by AFM. The white line in Fig. 1b indicates where the spectra were collected. The darker areas (0 nm) are still part of the cellular membrane but are of cell membrane regions only covering the cytoplasm, and not of that covering the nucleus, where the overall thickness is thus regarded as more thin. From the AFM image, an intact cell membrane was clearly visualized at this time point. The cytoplasmic regions were largely devoid of lipid inclusions surrounding the nucleus and nuclear envelope, located predominately where the regions of high topography were detected (see bright regions in Fig. 1a). At this time point, the cytoplasmic region is also more condensed around the nucleus, as polarization reflected in the cell morphology has not yet manifested.

TERS spectra were obtained at different points on the membrane every 150 nm. In contrast to conventional Raman spectroscopy, where spectra from the whole cell volume in the laser focus are measured, TERS exclusively provides the chemical information of molecules closest in vicinity to the tip. The collected spectra were very diverse, as expected when considering the composition of a cell membrane. Additionally, the signal-enhancing field at the tip apex decays exponentially, thus limiting the z-axis detection to a few nanometers at most, i.e., only the first cell layer characterization. All TERS measurements presented here were from line scans.

Detected features within the average spectrum of 26 spectra displayed in Fig. 2 indicated the presence of varying protein (amide I–III) and lipid components as the tip moved across the plasma membrane. The entire spectral dataset is given in ESM Fig. S2 (please note that absolute intensity variations in the average data are not considered due to the strong influence of feedback parameters and the tip-sample distance dependence of the signal).

Characteristic bands of proteins and lipids are highlighted in Fig. 2. Along the measured line, cysteine-rich (νCS around 804, 774, 750 cm^{-1}) and tyrosine-rich (ring breath around 852 cm^{-1}) areas were detected. Since no ester bands around

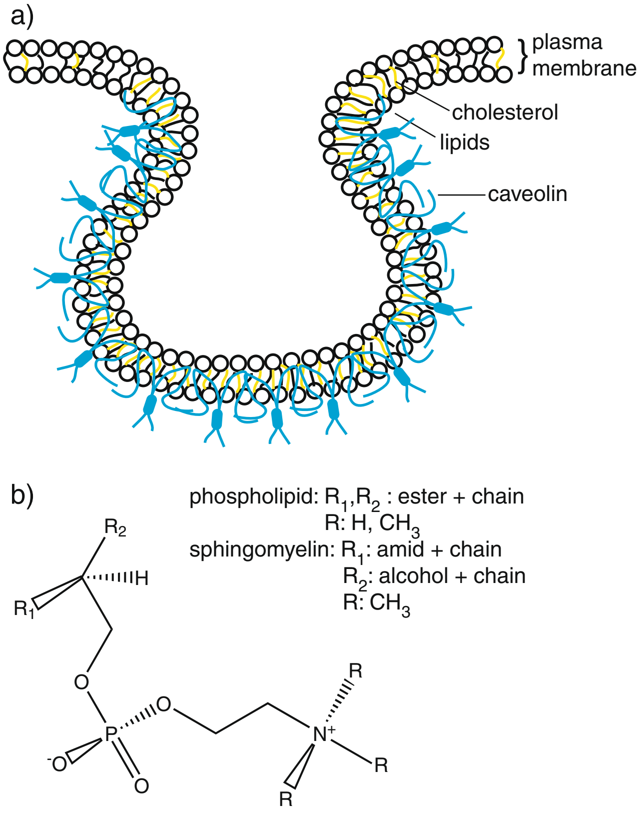

Fig. 3 Model of a caveolar bulb (**a**) and the molecular structures of associated phospholipids (**b**)

1,730 cm^{-1} were detected, the presence of phospholipids could be excluded at this specific cell locality. A small band at 725 cm^{-1} (νMe_3N^+–) pointed to sphingolipid content, but further separation (sphingomyelin versus glycosphingolipids) was not possible due to overlapping signals. Also, the broad band between 920 and 990 cm^{-1} (Si overtone) derives from the TERS tip. Each spectrum was assessed with respect to the presence of protein and lipid bands, and a map was generated as shown in Fig. 2 (top). It is evident that both membrane constituents were likewise detected (red: protein, green: lipid, blue: mixture of both), which is in agreement with previous TERS experiments on cells where lipid rafts were interspersed with proteins [22].

Here, the detected protein/lipid distribution is in agreement with the composition of a generic plasma membrane on an unactivated, unpolarized cell. In such cells, at 0 h post-wounding, widespread responses are not seen at the protein and lipid levels this soon post-wounding. The observed spectral fluctuations are also in agreement with the molecular orientation under the tip, as reported for other biological samples (see ref. [22, 23] for further information). Table 1 gives an assignment of the corresponding TERS signals.

The distribution of caveolar bulbs among cells 24 h post-wounding was then assessed and compared with that at 0 h. The presence of caveolae within the membrane allowed for easy identification, as these bulbs spanned approximately 50–120 nm in diameter and displayed a stable structure [10, 11]. Caveolae are thought to be involved in cell migration from their oriented distribution [6, 26] to assist with directional sensing of basal and granular layers of the epidermis during polarization [33]. Caveolar bulbs are also known to localize in the trailing edge of migrating endothelial cells, while cells migrating in 3-D display caveolar bulbs in a soluble, cytoplasmic form in the leading cell edges [6]. These inclusions can be

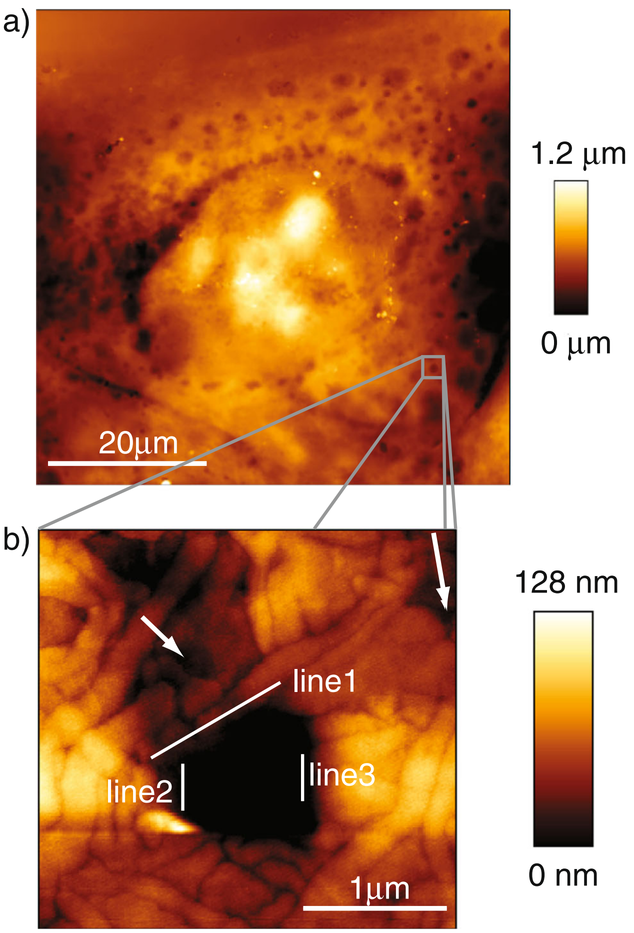

Fig. 4 **a** AFM topography of a caveolar bulb and its surrounding area on a HaCaT cell surface 24 h post-wounding; **b** enlarged image with *line 1*, *2*, and *3* showing the regions of TERS measurement. *0 nm* refers to the bottom of the caveolae. *Arrows* indicate smaller neighboring caveolae

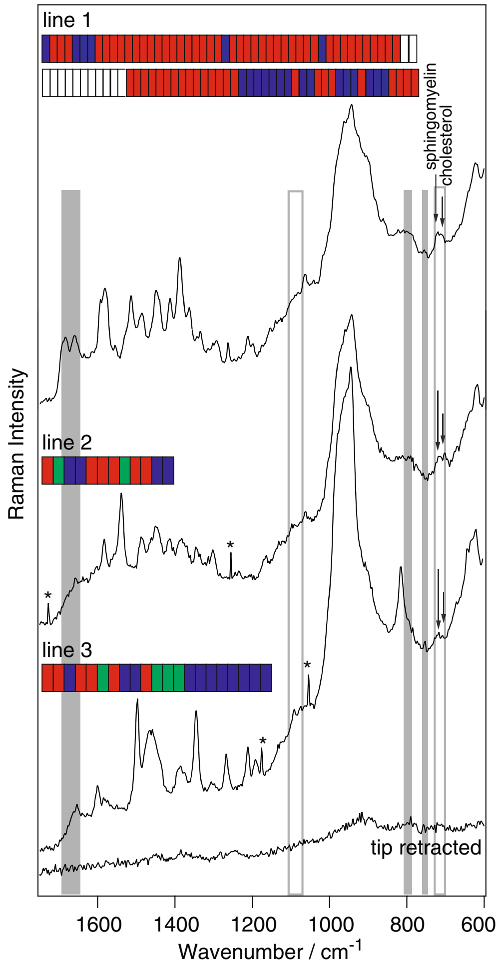

Fig. 5 TERS spectra of HaCaT cells 24 h post-wounding: *top* average spectrum of 72 raw spectra outside the caveolar bulb (*line 1* in Fig. 4b). Distance of measured points, 10 nm, t_{acu}=15 s; *middle* average spectrum of 12 raw spectra inside the caveolae (*line 2* in Fig. 4b); *bottom* average spectrum of 21 raw spectra inside the caveolae (*line 3* in Fig. 4b). Distance of measured points inside the caveolae, 25 nm, t_{acu}=15 s. The *colored maps* visualize the detection of proteins (*red*), lipids (*green*), and mixtures of both (*blue*) along the measured lines; *white pixels* lack of spectral information. Marker bands are highlighted; *grey line* protein, *rectangle* lipid. *Asterisks* indicate spikes due to cosmic rays. A reference spectrum of the cell was acquired (10 s) with the 500 µm retracted tip

found on most cell types, although they are particularly abundant in terminally differentiated cells like mature keratinocytes.

Caveolar bulbs are only formed in the presence of the caveolin protein through protein-protein interactions and are stabilized by caveolin oligomerization [13, 34, 35]. In the caveolar model (Fig. 3a), this clustering is depicted as an aggregate in the bow-shaped caveolin. More specifically, the caveolin-1 protein coating binds cholesterol tightly and selectively, enriching sterols in the area and maintaining the striated coat through hydrophobic interactions [8, 26, 36]. The lipid layer of caveolae consists of sphingolipids, particularly sphingomyelin, and glycosphingolipids [12, 13, 35, 36]. Sphingomyelin has a phosphocholine head group (Me_3N^+–) and two long alkyl chains with an amide and an alcohol residue (see Fig. 3b). For glycosphingolipids, the phosphocholine head group of sphingomyelin is replaced by a carbohydrate. Reports indicate that interactions of sphingomyelin with cholesterol are preferred over other phospholipids because of the stabilizing effect of the N-acyl group [37].

Until now, the characterization of this protein required isolation of caveolin-rich membrane domains from cells, which often inadvertently damages their structure [16, 36, 38]. Through AFM imaging, the localization of these microdomains in the cytoplasmic regions of the cell membrane is feasible. Their characteristic striated coatings were clearly visualized (see Fig. 4), despite the difficulties alternate techniques describe [7, 9]. At this time point, the cytoplasm has expanded from its previous, more condensed morphology in Fig. 1a. The distribution of the caveolin microdomains compared with the localization of the nucleus is clear and cell polarization has begun, with the leading cell edge possessing the majority of the caveolar bulbs present and nucleus being in a more proximal position to the cell monolayer.

The examined caveolin invagination was on the larger side—about 1 μm—but falls into the range of a "cycling" caveolin, during the "open" and "closed" states, instating a considerable range to this diameter size [12] and had a depth around 120 nm. As caveolar bulbs are not transmembrane structures, "0 nm" in the AFM scale bar refers to the bottom of the caveolar bulb. In addition to the measured

Table 2 Band assignments for TERS spectra on a HaCaT cell 24 h post wounding

Line 1	Line 2	Line 3	Assignment	Reference
1,696			C=O asym. str. (carboxyl, prot)	[22]
1,667, 1,647, 1,636	1,663, 1,652	1,654	Amide I (prot), C=C (lipid, cholesterol)	[22, 23, 29]
1,617, 1,590, 1,586	1,602, 1,596, 1,586	1,601, 1,577	C=C str. (prot, lipid, cholesterol)	[22, 23] [32]
1,556, 1,523	1,562, 1,539		Amide II, C=C str. (prot)	[22, 23] [28]
1,492	1,494	1,514, 1,502	CH_2, CH_3 def. (lipid, prot)	[22, 23]
1,485, 1,479	1,482, 1,464	1,479, 1,472, 1,466	CH, CH_2 def. (lipid, prot)	[22]
1,447, 1,438	1,448, 1,443	1,457, 1,437	CH_2, CH_3 def (lipid, prot, cholesterol)	[22, 23]
1,414, 1,406, 1,397, 1,387, 1,367, 1,335	1,413, 1,384, 1,375, 1,352, 1,345	1,393, 1,386, 1,353, 1,343	CH_2, CH_3 def. (lipid, prot)	[22, 23]
	1,314, 1,302	1,308	CH_2 twist (lipid, cholesterol)	[22, 23]
1,288	1,233	1,267, 1,257	Amide III, =CH bend, PO_2 asym. str. (lipid)	[22, 23]
1,211, 1,200		1,211, 1,187	CH_2, CC str., CH str. (prot)	[22, 23]
1,156	1,169		C–O str., COH bend (lipid)	[22, 23]
		1,133	CC str. (lipid)	[22]
1,065	1,063	1,091	C–C str., C–O str., PO_2 sym. str. (lipid)	[22, 23]
	1,006		Ring breath (phe, prot)	[22, 23]
990–920	990–920	990–920	Si overtone of tip	
858		855	Tyr	[22, 23]
		811	?	
		767	C–S str. (prot)	[22, 23]
725, 716		726	Me_3N^+ sym str. (sphingolipid)	[30, 31]
708	706	708	Ring breath (cholesterol)	[29, 32]
		641	?	[22, 23]
623	623, 614	617	Amide IV	

caveolar bulb, smaller caveolae were detected and are indicated with arrows.

Once caveolae were visualized, the TERS tip was aligned to investigate their surrounding striated regions for insight into the molecular composition. In Fig. 5 (top), an average TERS spectrum of 72 spectra (each 10 nm apart) of the measurement outside a caveolar bulb is depicted (line 1). For spectral information of the caveolar bulb itself, the tip was positioned in the cavity (line 2 and line 3 in Fig. 4b). Spectra in the middle and at the bottom of Fig. 5 display average TERS spectra of 12 and 21 spectra, respectively, from within the caveolae. On each line, the points were 25 nm apart. In the spectra, the characteristic bands of proteins, cholesterol, and sphingolipids were marked. The full spectral datasets are provided in ESM Figs. S3, S4, and S5.

Noticeable features specific for the presence of sphingolipids at 725 cm^{-1} (Me_3N^+–) and cholesterol at 705 cm^{-1} were detected in spectra outside and inside the caveolae. According to the abovementioned previous study [37], the lipid was supposed to be sphingomyelin but could not be further verified due to overlapping bands. The simultaneous detection of cholesterol was to be expected and confirms the results obtained from previous experiments [12, 13, 35, 36]. Table 2 displays the entire corresponding band assignment for the 24-h sample. All three spectral datasets of the measurements inside and outside the caveolar bulb were assessed with respect to the detection of proteins and lipids. The respective colored maps in Fig. 5 image the distribution of proteins (red), lipids (green), and mixtures of both (blue) along the measured lines. Evidently, the protein content on the 24-h cell membrane has elevated while lipid contribution has decreased compared to the 0-h cell, which was an indicator for the formation of caveolin. In contrast to the 0-h sample, no dominating signals for cysteine and tyrosine could be detected. From further studies, it is acknowledged that caveolin can be found not only inside the invagination but also outside [36].

Along the line outside the caveolae, bands of $COOH/COO^-$ groups were detected. Those bands are further good indicators of caveolin presence, whose sequence comprises 21 acidic amino acid residues, and have already been documented outside of caveolae [7, 36, 39]. From the spectra in Fig. 5, it is evident that no carboxyl bands were detected inside the caveolae. This might be attributed to an endocellular orientation of the hydrophilic side chains, leaving them out of reach of the TERS tip. Apart from that, no striking spectral differences between the inside and outside of the caveolae were identified. These presented data are also a first approach towards full cell invagination characterization and warrant further TERS study for a complete and thorough chemical profile. Moreover, it could be clearly demonstrated that chemical changes induced by wound healing can already be detected on the nanoscale. In other words, TERS enables the visualization of cell migratory effects before conventional microscopic techniques can.

Immunofluorescence

The identical cells from the TERS measurements were tagged with FITC-labeled (green) anti-caveolin1 (CAV1) and DAPI (blue) post-TERS analysis. This enabled the visualization of CAV1 distribution during cell polarization in the red region of interest (see ESM Fig. S6). Immunofluorescence was found to illustrate that at 0 h, CAV1 was localized within the cell cytoplasm, largely surrounding the nucleus (see ESM Fig. S6, top). This is in agreement with previous findings, as oligomerization of the caveolin protein occurs within the endoplasmic reticulum [7] and largely no caveolae were detected on the cell surface at 0 h through AFM imaging. By 24 h, the localization of CAV1 through immunofluorescence was noticed to shift to a distribution either on the plasma membrane or more close to it (see ESM Fig. S6, bottom), in agreement with previous observations [40, 41] and further supporting our AFM topographical conclusions.

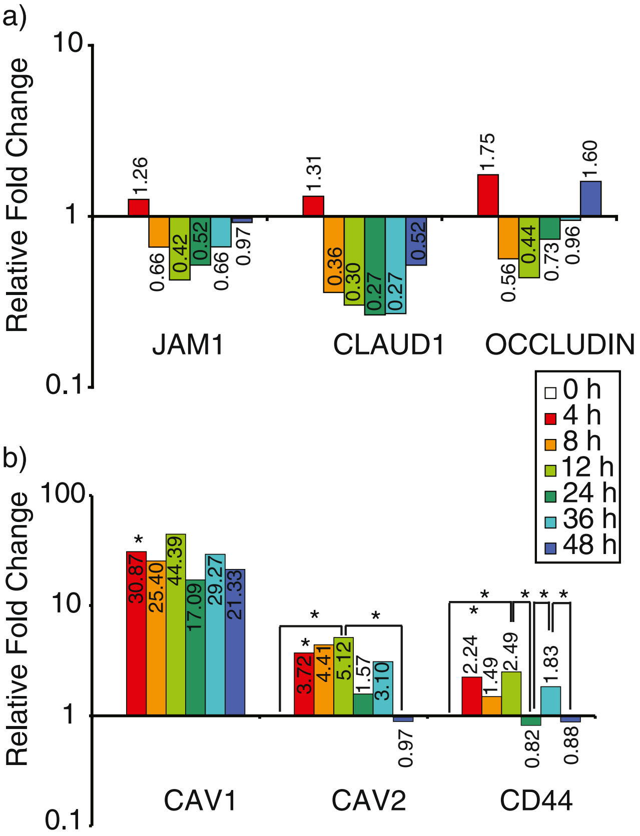

Fig. 6 **a** Transcript expressions for OCCLUD, CLAUD1, and JAM1 profiles related to tight junction presence-stimulated wound healing expression; **b** transcript expression profiles of CAV1, CAV2, and CD44. Significance was tested using the Mann-Whitney *U* nonparametric test, where $p \leq 0.10$, and all time points were compared with 0 h as the baseline at 1

RT-qPCR

RT-qPCR was applied to further confirm the alterations in cell activity between 0 and 24 h. Of particular importance were tight junctions because cells must loosen attachments to one another for polarization and subsequent migration. The gene expression of transcripts for proteins involved in tight junctions, including occludin (OCCLUD), junctional adhesion molecule 1 (JAM1), and claudin 1 (CLAUD1), was explored over both time points (see Fig. 6a). As anticipated, transcript expression of all tight junction genes was downregulated following sample wounding to facilitate morphological changes between 8 and 36 h post-stimulated wounding. From 24 to 48 h, expression increased as cell migration subsided and polarization became less necessary, resuming original cell contact for communication and structural integrity.

The transcript expression profile for caveolin-1 (CAV1) and caveolin-2 (CAV2) was explored for their role in caveolae structural formation [7, 42] and CD44 (cluster of differentiation no. 44; involved in lipid synthesis) based on its involvement in cholesterol synthesis. Following stimulated wounding, transcript expressions of CAV1 and CAV2 were upregulated for the duration of the cell migration, in agreement with AFM (and immunofluorescence results) (see Fig. 6b). Caveolae signaling is regulated by CAV1 and CAV2 during wound healing. As polarization and migration begin to subside by 24 h, CAV2 expression downregulates while CAV1 expression remains relatively stable indicating overall wound healing efficiency, which is consistent with associated literature [43]. CD44 was found upregulated and displayed an expression profile similar to that of CAV2, indicating cholesterol synthesis occurred in wounding onset but diminished as overall migration and cell polarization were no longer necessary as well.

Conclusion

For the first time, simultaneous topographical and label-free structural characterization on the nanometer scale of individual cell caveolar bulbs was facilitated using TERS and during differing time points post-wounding to better understand caveolar bulb distributions and fluctuations during wound healing. To elucidate changes on the membrane, AFM topographical images and spectra were collected immediately following (0 h) and 24 h after wounding. As a result, insight into the structure and distribution of caveolae was obtained without the need for labeling or separation techniques. Furthermore, all AFM and spectroscopic results were verified through RT-qPCR analysis and immunofluorescence, spanning transcript and protein levels.

In summary, current results clearly qualify TERS as a valuable tool for general and specific label-free lipid target analysis, particularly on in-depth studies pertaining to individual microdomains. As underlying mechanisms of cell polarization remain to be thoroughly elucidated, this nondestructive structural insight can provide information able to identify potential binding regions within caveolar bulbs and their associated downstream effects resulting in cell polarization and morphology. The intrinsic specificity and high spatial resolution capabilities of TERS not only enable the differentiation of membrane components but give access to questions like wound healing defects or interactions with vulnerary drugs.

Acknowledgments We thank the Bundesministerium für Bildung und Forschung (No. 0312032B and No. 0312032C) for their financial support.

References

1. Bryant DM, Mostov KE (2008) From cells to organs: building polarized tissue. Nat Rev Mol Cell Biol 8:887–901
2. Conti MA, Adelstein RS (2008) Nonmuscle myosin II moves in new directions. J Cell Sci 121:11–18
3. Olguin P, Mlodzik M (2010) A new spin on planar cell polarity. Cell 142:674–676
4. Gniadecki R, Bang B (2003) Flotillas of lipid rafts in transit amplifying cell-like keratinocytes. J Investig Dermatol 121:522–528
5. Shaul PW, Anderson RG (1998) Role of plasmalemmal caveolae in signal transduction. Am J Physiol 275:L843–L851
6. Navarro A, Anand-Apte B, Parat MO (2004) A role for caveolae in cell migration. FASEB J 18:1801–1811
7. Lajoie P, Nabi IR (2010) Lipid rafts, caveolae, and their endocytosis. Int Rev Cell Mol Biol 282:135–163
8. Williams TM, Lisanti MP (2004) The caveolin proteins. Genome Biol 5:214.211–241.215
9. Rothberg G, Heuser J, Donzell W, Ying Y-S, Glenney JR, Anderson R (1992) Caveolin, a protein component of caveolae membrane coat. Cell 68:673–682
10. Wang Z, Tiruppathi C, Minshall RD, Malik AB (2009) Size and dynamics of caveolae studied using nanoparticles in living endothelial cells. Nano 3:4110–4116
11. Lucius H, Friedrichson T, Kurzchialia T, Lewin G (2003) Identification of caveolae-like structures on the surface of intact cells using scanning force microscopy. J Membr Biol 194:97–108
12. Razani B, Woodman SE, Lisanti MP (2002) Caveolae: from cell biology to animal physiology. Pharmacol Rev 54:431–467
13. Stan RV (2005) Structure of caveolae. Biochim Biophys Acta 1746: 334–348
14. Kenworthy A (2002) Peering inside lipid rafts and caveolae. Trends Biochem Sci 27:435–437
15. Kuerschner L, Ejsing CS, Ekroos K, Shevchenko A, Anderson KI, Thiele C (2005) Polyene-lipids: a new tool to image lipids. Nat Methods 2:39–45
16. Zheng Y, Foster J (2009) Contribution of quantitative proteomics to understanding membrane microdomains. J Lipid Res 50:1976–1985
17. Cialla D, März A, Böhme R, Theil F, Weber K, Schmitt M, Popp J (2012) Surface-enhanced Raman spectroscopy (SERS): progress and trends. Anal Bioanal Chem 403:27–54

18. Willets KA, Van Duyne P (2007) Localized surface plasmon resonance spectroscopy and sensing. Annu Rev Phys Chem 58:267–297
19. Pozzi EA, Sonntag MD, Jiang N, Klingsporn JM, Hersam MC, Van Duyne P (2013) Tip-enhanced Raman imaging: an emergent tool for probing biology at the nanoscale. ACS Nano 7:885–888
20. Pettinger B, Schambach P, Villagomez CJ, Scott N (2012) Tip-enhanced Raman spectroscopy: near-fields acting on a few molecules. Annu Rev Phys Chem 63:379–399
21. Bailo E, Deckert V (2008) Tip-enhanced Raman scattering. Chem Soc Rev 37:921–930
22. Richter M, Hedegaard M, Deckert-Gaudig T, Lampen P, Deckert V (2011) Laterally resolved and direct spectroscopic evidence of nanometer-sized lipid and protein domains on a single cell. Small 7:209–214
23. Deckert-Gaudig T, Böhme R, Freier E, Sebesta A, Merkendorf T, Popp J, Gerwert K, Deckert V (2012) Nanoscale distinction of membrane patches—a TERS study of Halobacterium salinarum. J Biophoton 5:582–591
24. Cialla D, Deckert-Gaudig T, Budich C, Laue M, Möller R, Naumann D, Deckert V, Popp J (2009) Raman to the limit: tip-enhanced Raman spectroscopic investigations of a single tobacco mosaic virus. J Raman Spectrosc 40:240–243
25. Vandesompele J, De Preter K, Pattyn F, Poppe B, Van Roy N, De Paepe A, Speleman F (2002) Accurate normalization of real-time quantitative RT-PCR data by geometric averaging of multiple internal control genes. Genome Biol 3:RESEARCH0034
26. Grande-García A, del Pozo M (2008) Caveolin-1 in cell polarization and directional migration. Eur J Cell Biol 87:641–647
27. Gomez-Mouton C, Lacalle RA, Mira E, Jimenez-Baranda S, Barber DF, Carrera AC, Martinez AC, Manes S (2004) Dynamic redistribution of raft domains as an organizing platform for signaling during cell chemotaxis. J Cell Biol 164:759–768
28. Böhme R, Cialla D, Richter M, Rösch P, Popp J, Deckert J (2010) Biochemical imaging below the diffraction limit—probing cellular membrane related structures by tip-enhanced Raman spectroscopy (TERS). J Biophoton 3:455–461
29. Krafft C, Knetschke T, Siegner A, Funk RHW, Salzer R (2003) Mapping of single cells by near infrared Raman microscopy. Vib Spectrosc 32:75–83
30. Lamba OP, Borchman D, Sinha SK, Lal S, Yappert MC, Lou MF (1991) Structure and molecular conformation of anhydrous and aqueous sphingomyelin bilayers determined by infrared and Raman spectroscopy. J Mol Struct 248:1–24
31. Borchman D, Tang D, Yappert MC (1999) Lipid composition, membrane structure relationships in lens and muscle sarcoplasmic reticulum membranes. Biospectroscopy 5:151–167
32. Faiman R (1977) Raman spectroscopic studies of different forms of cholesterol and its derivatives in the crystalline state. Chem Phys Lipids 18:84–104
33. Sando GN, Zhu H, Weis JM, Richman JT, Wertz PW, Madison KC (2003) Caveolin expression and localization in human keratinocytes suggest a role in lamellar granule biogenesis. J Investig Dermatol 120:531–541
34. Quest AFG, Leyton L, Párraga M (2004) Caveolins, caveolae, and lipid rafts in cellular transport, signaling, and disease. Biochem Cell Biol 82:129–144
35. Epand RM, Sayer BG, Epand RF (2005) Caveolin scaffolding region and cholesterol-rich domains in membranes. J Mol Biol 345:339–350
36. Sonnino S, Prinetti A (2009) Sphingolipids and membrane environments for caveolin. Fed Eur Biochem Soc 583:597–606
37. Ramstedt B, Slotte JP (2006) Sphingolipids and the formation of sterol-enriched ordered membrane domains. Biochim Biophys Acta 1758:1945–1956
38. Lisantti MP, Scherer PE, Vidugiriene J, Tang Z, Hermanowski-Vosatka A, Tu YH, Cook RF, Sargiacomo M (1994) Characterization of caveolin-rich membrane domains isolated from an endothelial-rich source: implications for human disease. J Cell Biol 126:111–126
39. Li S, Seitz R, Lisanti MP (1996) Phosphorylation of caveolin by Src tyrosine kinases. J Biol Chem 271:3863–3868
40. Tagawa A, Mezzacasa A, Hayer A, Longatti A, Pelkmans L, Helenius A (2005) Assembly and trafficking of caveolar domains in the cell: caveolae as stable, cargo-triggered, vesicular transporters. J Cell Biol 170:769–779
41. Li WP, Liu P, Pilcher BK, Anderson RG (2001) Cell-specific targeting of caveolin-1 to caveolae, secretory vesicles, cytoplasm or mitochondria. J Cell Sci 114:1397–1408
42. Langlois S, Cowan KN, Shao Q, Cowan BJ, Laird DW (2008) Caveolin-1 and -2 interact with connexin43 and regulate gap junctional intercellular communication in keratinocytes. Mol Biol Cell 19:912–928
43. Rhim JH, Kim JH, Yeo EJ, Kim JC, Park SC (2010) Caveolin-1 as a novel indicator of wound-healing capacity in aged human corneal epithelium. Mol Med 16:527–534